IEEE Access
Multidisciplinary | Rapid Review | Open Access Journal

Received 8 October 2024, accepted 9 December 2024, date of publication 12 December 2024, date of current version 20 December 2024.

Digital Object Identifier 10.1109/ACCESS.2024.3516380

RESEARCH ARTICLE

A Two-Step Inverse Algorithm for Biomedical Magnetic Induction Tomography With Neural Networks: Introduction and Error Analysis

ANNA HOFMANN, MORITZ FEHR, AND ANDREAS SAUER
Institute of Natural Sciences, University of Applied Sciences Ruhr West, 45479 Mülheim, Germany
Corresponding author: Anna Hofmann (anna.hofmann@hs-ruhrwest.de)

ABSTRACT Medical imaging is a continuously evolving field with a constant need for advancements in its capabilities and applications. Magnetic induction tomography (MIT) represents a promising alternative to the established imaging methods. MIT is a non-invasive and cost-effective tomography method with considerable potential for biomedical imaging. Nevertheless, the inverse problem associated with MIT is inherently difficult to resolve using conventional techniques, primarily due to its ill-conditioned and nonlinear nature. The application of machine learning methods offers an elegant solution to the image reconstruction process. In contrast with the conventional approach of directly reconstructing images from measured signals, the inverse algorithm proposed here is divided into two subproblems. This approach was inspired by the physics of the forward problem. Specifically, the underlying currents are first reconstructed from the signals and then the conductivity distribution is reconstructed from those in the second step. For each of those problems, specifically designed neural networks were employed. This approach demonstrated very good reconstruction quality, as evidenced by excellent metrics on the test dataset, which differed significantly from the training data. Furthermore, an extensive error analysis was conducted to identify the strengths and weaknesses of the image reconstruction process.

INDEX TERMS Deep learning, image reconstruction, inverse problems, magnetic induction tomography.

I. INTRODUCTION

Imaging techniques are key diagnostic tools used in modern medicine. Among these techniques is magnetic induction tomography (MIT), which was first introduced in the early 1990s [1] and is currently in the basic research stage for applications in the medical field. Consequently, it is undergoing constant technical changes.

Its principle is based on electrodynamics: An alternating current flows through a transmitter coil, thereby generating a magnetic field. According to Faraday's law, this magnetic field induces an electric field, which we refer to as the primary field. This primary field generates eddy currents in the object under examination. The density of these eddy currents depends on the conductivity distribution of the object. Again, based on Faraday's law, a secondary electric field is generated by the alternating eddy currents, which can then be measured by receiver coils. The objective of MIT is to reconstruct the conductivity distribution in the body using these measured signals.

Therefore, MIT is a noninvasive, contactless tomography method that can be used for biomedical imaging. Potential applications include lung diagnosis [2], detection of brain hemorrhages [3], and cancer diagnosis and treatment [4].

Classical MIT setups use a transmitter and receiver geometry similar to that of computed tomography (CT), with the transmitter and receiver arranged in a circular order around the object to be examined. However, these setups frequently suffer from low central-area sensitivity in voluminous bodies, which can present a significant challenge for medical applications. A planar design has demonstrated a

The associate editor coordinating the review of this manuscript and approving it for publication was Roberta Palmeri.

notable enhancement in sensitivity in the central area of the body [5].

Similar to other tomography methods, MIT has a forward and an inverse problem. The forward problem describes the physical relations based on Maxwell's equations for receiving a measured signal from the body under examination. The inverse problem consists of reconstructing the original conductivity distribution of the body, starting from a measured signal. Usually, these reconstructions are of low resolution because of the dispersed nature of the magnetic fields [1].

One of the primary challenges of MIT is finding a solution to the inverse problem. It suffers from ill-conditioning, meaning that only small disturbances in the measured signal can cause large reconstruction errors [1]. In particular, the conductivity distribution of voluminous bodies in a biomedical setup is difficult to reconstruct [5]. There are various mathematical tools to solve the inverse problem, including regularization techniques such as Tikhonov regularization [6] and classical approximation methods such as Gauss-Newton [7]. However, the resulting images often exhibit artifacts or significant error margins. Moreover, the mathematical properties of image reconstruction in MIT remain an active area of investigation and have yet to be fully resolved.

Recently, another innovative approach for solving inverse problems in imaging has received increasing attention. The application of machine learning techniques, particularly neural networks, has led to remarkable outcomes in image reconstruction across diverse tomography methods. This approach has been applied in a number of different contexts, including direct image reconstruction [8], improvement of classical image reconstructions through denoising [9], and super-resolution [10]. In MIT, most applications are for the direct image reconstruction. In order to achieve this, a variety of different architectures have been employed, including residual neural networks (ResNets) [11], autoencoders (AEs) [12], and generative adversarial networks (GANs) [13]. These have demonstrated very good potential for solving the inverse problem. Each of these approaches uses a direct image reconstruction from the signal to the conductivity distribution. Consequently, the physical properties of the forward problem are not considered.

In this study, the direct image reconstruction process is divided into two subproblems, which are inspired by the forward problem calculation. A similar approach using analytical algorithms and four subdivisions has been investigated in [14]. Here, the first subproblem involves reconstructing the eddy currents of the body being examined from the measured signals. The second subproblem involves determining the original conductivity distribution from these eddy currents. Specific neural networks have been trained for each of these subproblems. This division into subproblems offers multiple advantages. The individual subproblems can be directly replaced with analytical algorithms or different neural network architectures. It also facilitates better control and insights of the individual neural networks, making it easier to identify the causes of reconstruction errors and artifacts.

Furthermore, the use of two measurements instead of one resulted in significantly improved convergence. To achieve this, the body was measured, rotated by 180 degrees, and measured again. The conductivities of these two signals were then reconstructed and combined to create an overall reconstruction. The combined reconstructions demonstrated excellent metrics across the entire test dataset, despite the test dataset differing significantly from the training data. This indicates a robust generalization ability of the reconstruction process with the division into two subproblems. This finding is supported by a comprehensive error analysis.

II. METHODS

A. PROBLEM DEFINITION

The MIT configuration used here has a planar design, as previously investigated in [5]. The transmitter, called the undulator, is positioned on one side and consists of eleven vertically aligned parallel wires with an antiparallel current flow. An alternating, sinusoidal current with a frequency of 1.5 MHz is used. The receivers are positioned on the opposite side with a butterfly shaped form in a gradiometric position. With this positioning, the primary field of the undulator is not measured. The complete receiver array consists of three wide and three narrow receivers vertically stacked on top of each other. The object under examination traverses a distance of 256 cm between the undulator and the receiver array, which results in a signal being measured by each of the six receivers, as illustrated in Fig. 1.

This specific configuration exhibited a considerable improvement in sensitivity within the central region of the examined body. Reconstructions of the original conductivity distribution of a voluminous body in a biomedical context improved tremendously with this new setup, as evidenced by [5].

B. THE FORWARD PROBLEM

The rather simple connections in the forward problem are a major advantage of MIT with planar design. The underlying physics can be readily described using Maxwell's equations. Due to the alternating current flow in the undulator, an alternating magnetic field is induced. The magnetic flux density $\boldsymbol{B}$ of the undulator can be described by the rotation of the magnetic vector potential as follows:

$$\nabla \times \boldsymbol{A} = \boldsymbol{B}. \tag{1}$$

In this MIT setup, only straight wires are used as receivers and transmitters; therefore, the magnetic vector potential of all relevant magnetic fields can be calculated explicitly using Biot-Savart's law [15]. To clarify, if a finite thread is positioned at point (x, y_1, z) and extends to point (x, y_2, z)

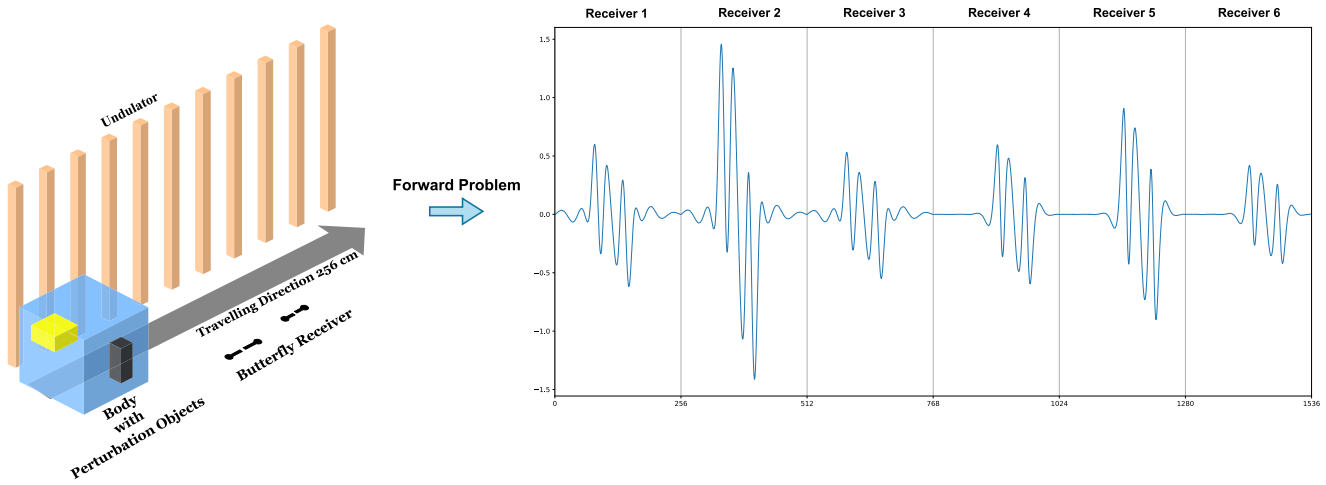

FIGURE 1. Geometry of the planar MIT setup. In the forward problem, a voluminous body travels 256 cm between the undulating exciter and receiver, which results in a signal being measured. In the inverse problem, the measured signal is used to reconstruct the conductivity distribution of the original body.

with a current I, the vector potential $\boldsymbol{A}$ is then given by the following formula:

$$\boldsymbol{A}_y(x, y, z) = \frac{\mu_0 I}{4\pi} \cdot \log \frac{(y_2 - y) + \sqrt{(y_2 - y)^2 + x^2 + z^2)}}{(y_1 - y) + \sqrt{(y_1 - y)^2 + x^2 + z^2)}}. \tag{2}$$

Similarly, for any straight wire connected to arbitrary points, the vector potential can be equivalently calculated. The vector potential of the undulator and receivers can be expressed by appropriate superpositions of the aforementioned formulae.

For additional calculations, the body under examination must be discretized. Here, it is subdivided into cuboid voxels. The electric currents within the body are then represented by the currents in an electrical network connected to the center of each voxel. The magnetic vector potential then generates a reactive scalar potential φ in the body at each midpoint of a voxel. This vector potential is calculated by solving a system of linear equations, which follows from classical nodal analysis in electrical networks.

By using Ohm's law, the eddy current $\boldsymbol{I}$ can be calculated at each of the 256 measuring positions. Because the undulator creates a sinusoidally periodic excitation field, only two positions must be effectively calculated. The first position, namely Φ, is located directly in front of one of the undulator coils, whereas the other position Ψ is located in the middle between two undulator coils. The current at each measuring point $x_1 = 1, \ldots, x_n = 256$ can then be calculated via superposition using the following formula [5], [14]

$$\boldsymbol{I}_{x_k} = \sin\left(\frac{2\pi x_k}{D}\right)\boldsymbol{I}_\Phi + \cos\left(\frac{2\pi x_k}{D}\right)\boldsymbol{I}_\Psi, \quad k = 1, \ldots, 256 \tag{3}$$

where D is the distance between two undulator conductors in the same current direction. In this setup, D is set to 48 cm. Finally, the resulting signal is determined using the Lorentz-reciprocity [16]:

$$S \approx \sum_{k=1}^{n} \boldsymbol{I}_k \cdot (\boldsymbol{A}_R)_k \cdot \Delta l \tag{4}$$

where $\boldsymbol{A}_R$ is the vector potential of the receivers at voxel k, Δl is the voxel size of the grid, and n is the number of voxels in the body. The signal is determined at 256 positions by six receivers and consists of $1536 = 256 \cdot 6$ measured values.

In summary, the discretized forward problem can be described by the following mapping:

$$F : [0, 1]^n \to \mathbb{R}^m, \quad F : \sigma \mapsto S \tag{5}$$

where σ is the conductivity of the given body discretized into n voxels with $0 \leq \sigma \leq 1$ and m the length of the signal S.

C. TWO-STEP INVERSE ALGORITHM

The forward problem (5) describes the process from the conductivity distribution to the measured signal. This can be described as two subproblems derived from equations (3), (4), and (5). Initially, based on the given conductivity, the eddy currents at each measuring position are calculated using the formula (3). Subsequently, the signal is determined using (4). This can be defined as two subproblems, which can be expressed as the following discretized mappings:

$$F_1 : [0, 1]^n \to \mathbb{R}^{6 \cdot n}, \sigma \mapsto (\boldsymbol{I}_\Phi, \boldsymbol{I}_\Psi) \tag{6}$$

$$F_2 : \mathbb{R}^{6 \cdot n} \to \mathbb{R}^m, (\boldsymbol{I}_\Phi, \boldsymbol{I}_\Psi) \mapsto S. \tag{7}$$

Here, σ is the given conductivity distribution of the body discretized into n voxels; $(\boldsymbol{I}_\Phi, \boldsymbol{I}_\Psi)$ are the eddy currents at positions Φ and Ψ of the discretized body at each node of a voxel; and S is the calculated signal over m measuring positions.

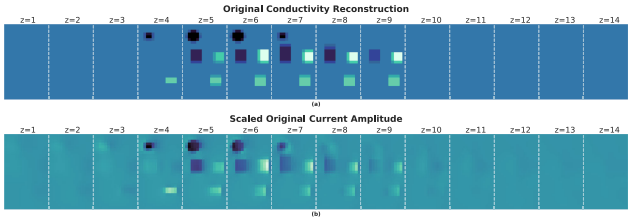

FIGURE 2. Comparison of the original conductivity distribution (a) and the original standard scaled current amplitude (b). The perturbation objects can already be spotted in the scaled current amplitude. It can also be seen how perturbation objects disturb the current flow in the body.

In the classical approach, the inverse problem determines the conductivity distribution σ from the measured signal S. Based on the forward chain (6)-(7), the inverse problem can also be divided into similar subproblems. Starting from a signal S, the eddy currents $\boldsymbol{I}_\Phi$ and $\boldsymbol{I}_\Psi$ are determined. However, these are two vector fields, and thus not practical for a reconstruction with neural networks due to the large number of neurons required. Based on the alternating current theory, eddy currents can be summarized using the current amplitude. The current amplitude is the L2-norm of the currents over a period of time:

$$I_A^k = \sqrt{(\boldsymbol{I}_\Phi^k)^2 + (\boldsymbol{I}_\Psi^k)^2}, \quad k = 1, \ldots, n. \tag{8}$$

In consequence, the first subproblem is the reconstruction of the current amplitude from the signal. The second step of the inversion is to calculate the conductivity distribution from the current amplitude. Although nonlinear, this subproblem can be readily determined even with analytical algorithms, as demonstrated in previous studies (e.g., [14]). If the current amplitude is appropriately scaled, for instance using a standard scaler based on the training data, the underlying conductivity distribution can be observed from the current amplitude when plotted (see Fig. 2).

In summary, the two-step inverse algorithm can be described as a composed mapping $S \mapsto I_A \mapsto \sigma$. The advantage of this approach is that each problem can be solved individually, as demonstrated in the following section, through the use of neural networks.

D. THE NEURAL NETWORKS

Two separate neural networks are used to solve the two-step inverse algorithm. The reconstruction of the current amplitude is based on a supervised autoencoder (sAE), similar to that introduced in [17]. In the second part of the inverse algorithm, the conductivity distribution is reconstructed from the current amplitude using a residual neural network (ResNet).

1) THE SUPERVISED AUTOENCODER (sAE)

A supervised autoencoder integrates the essential elements of both autoencoder and supervised learning paradigms. In essence, an autoencoder comprises two primary components: the encoder, which performs an unsupervised transformation of the input data into a lower-dimensional representation, or latent space; and the decoder, which, from this compressed space, reverses the output of the hidden layer to yield the reconstructed input. Autoencoders have a variety of applications, including data denoising, dimensionality reduction, feature learning, data compression, and image generation [18]. The integration of supervisory elements into the training process has been shown to be beneficial, as evidenced by the findings of [17] and [19]. This approach enables the model to learn and encode not only the reconstruction (as in a traditional autoencoder), but also the task-specific supervised output. The loss function to be minimized includes both reconstruction loss and task-specific loss (see Fig. 3). In this manner, the reconstruction error acts as a regularizer for the supervised part of the loss. Furthermore, this ability allows the relationship between the input and output to be learned and generalized, thereby enhancing the model's predictive capabilities.

In this approach, the current amplitude (the specific task) was obtained by utilizing the fundamental concept of the supervised autoencoder, augmented with further modifications and refinements to the network architecture. The decoder and encoder components of the network were constructed using four 2D convolutional layers consisting of various specific channels and filter sizes. The base components end or start with two fully connected dense layers, with the latent space situated between them. The autoencoding component of the network ensures that the signal reconstruction process is learned.

Furthermore, the latent space is fed into the supervised component through a minor branch of fully connected dense layers, where the current amplitude is learned simultaneously (Fig. 3). To refine the output, a straightforward four-layer denoising autoencoder structure was employed, which was integrated into the training process. The implementation of this straightforward measure led to a notable enhancement in the reconstruction quality. The number of layers was methodically selected; however, the potential range of layers was constrained due to the inclusion of the denoising autoencoder in the training process and its dependence on the input size.

A global criterion is defined that combines the reconstruction losses. This is composed of the sum of the different losses and is then used to minimize the error of the complete model. The weighting factors can also be used as hyperparameters to adjust the learning of the two different parts of the model. The optimal training outcomes were achieved through the utilization of an equally weighted sum of the loss function (Mean Absolute Error).

2) THE RESNET

The reconstructed current amplitudes can be visualized as an image, which is subsequently transformed into the underlying conductivity distribution. As illustrated in Fig. 2,

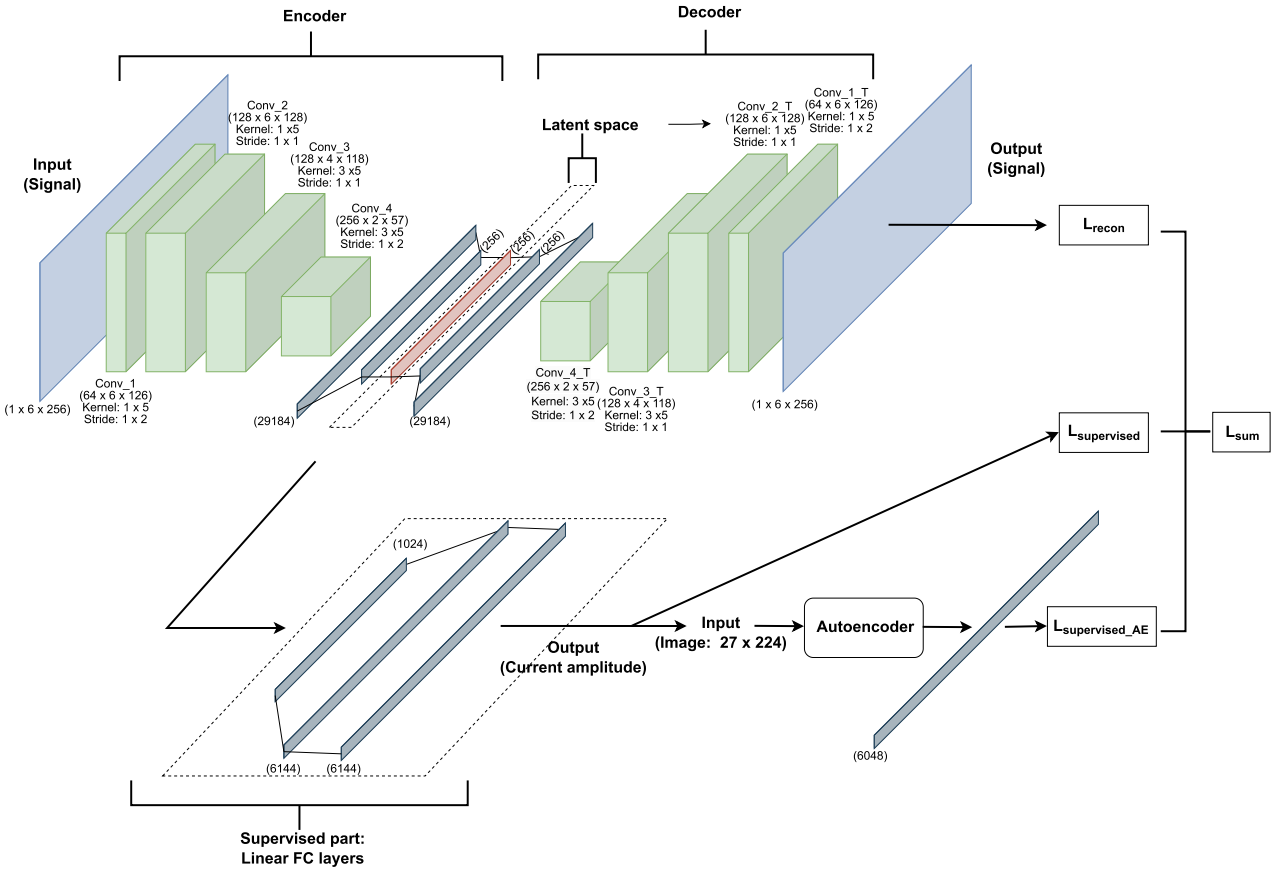

FIGURE 3. Architecture of a supervised autoencoder neural network. This figure presents the design of a supervised autoencoder, which is composed of an encoder and decoder with a supervised component in between. Furthermore, the network is augmented with a standard autoencoder for output smoothing and denoising, which is not shown in detail here. The dimensions of each convolutional layer, including the size of the kernel, the stride, and the padding, as well as the size of each dense layer, are explicitly indicated. Additionally, the figure illustrates the various loss functions employed, including the reconstruction loss function, denoted as L_{recon}, the supervised loss function, denoted as $L_{supervised}$, the supervised AE loss function, denoted as $L_{supervised\_AE}$ and the overall loss function, denoted as L_{sum}. These loss functions are used for signal reconstruction, the raw and smoothed reconstruction of the current amplitude and the weighted overall combination of the loss functions.

the standardized scaled current amplitudes and the conductivity distribution exhibit a high degree of similarity. Consequently, the utilization of a neural network comprising convolutional layers was found to be advantageous. To further reduce the complexity of the network and the number of parameters used, a residual neural network was employed to reconstruct the conductivity distribution from the current amplitudes.

In detail, the current amplitude is reshaped into a two-dimensional image, as shown in Fig. 2. This is followed by four bottleneck layers. Each bottleneck layer comprises three convolutional layers, constructed in accordance with the methodology outlined in the original ResNet study [20], with the objective of reducing the input size. Following the classical average pooling layer, two dense layers with sigmoid activation were used. In order to prevent overfitting, two dropout layers were utilized, with 20% of neurons randomly being dropped. The final layer comprises 6,048 neurons with a hard sigmoid activation function, which reconstructs the conductivity distribution between 0 and 1 for each voxel. Fig. 4 provides a detailed overview of the complete residual neural network.

The ResNet was trained with the Huber loss, utilizing a $\delta = 0.5$ value over 100 epochs and a batch size of 512. As optimizer, Adam was utilized with a learning rate of 0.001.

E. DATASETS

1) TRAINING DATA

The training data were generated through the discretized forward problem of the planar MIT setup. As demonstrated in references [5] and [11], the discrepancies between the actual and simulated measurements are minimal, indicating that a dataset based on simulated data can also be suitable for real measurements.

The dimensions of the basic body of this dataset are 54 cm $\times$32 cm $\times$14 cm. The body was divided into voxels of a uniform size, each measuring 1 cm. Each voxel was initially assigned a conductivity of 0.5 S/m.

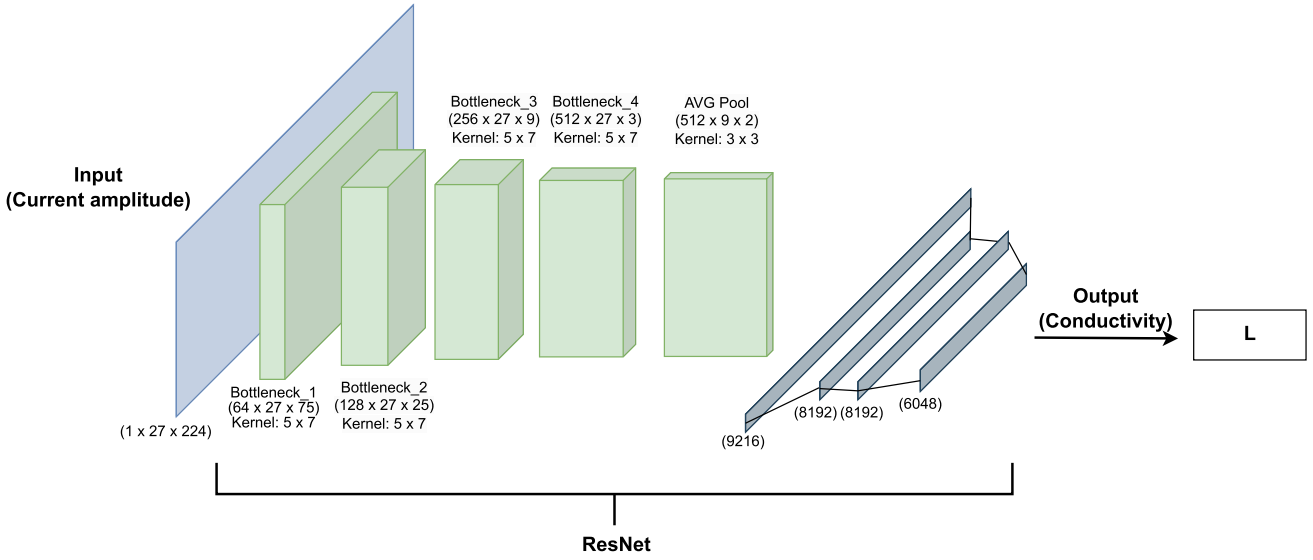

FIGURE 4. The residual neural network. Multiple bottleneck layers were used to reduce the input size given by the current amplitude reshaped as a two-dimensional picture. Each neuron of the output represents one voxel of the discretized body.

Cuboid perturbation objects with lengths between 6 and 10 cm were randomly inserted into this body without overlapping. The conductivities of these perturbation objects were randomly selected from the set $\sigma \in \{0, 0.25, 0.75, 1.0\}$. In total, up to five of those perturbation objects can be placed into the body, with a 1 cm gap to the boundaries of the body.

In order to accommodate the growing complexity of the reconstructions as the number of perturbation objects increases, the number of samples per number of perturbation objects was increased. In total, 760,000 data samples were created, and a detailed enumeration of the number of perturbation objects is presented in Table 1.

After placing the perturbation objects in the body, the associated eddy currents (and their respective current amplitudes) and signals were calculated. A noise level was randomly selected between 50 and 100 dB and added to each signal.

In order to prevent the inverse crime, the reconstruction of the current amplitudes and conductivity distribution was conducted on a coarser grid of 2 cm voxels. Consequently, the edges of the perturbation objects in the reconstruction are not clearly delineated from the background conductivity. The total number of voxels on the 2 cm grid is 6048 voxels. For the training process of the neural networks, the data was preprocessed:

1) The input signals of each receiver were filtered using a standard fifth-order Butterworth filter.
2) The ground truth data for the current amplitudes were multiplied by a factor of 10^6 and subsequently scaled with min-max feature scaling.
3) A separate dataset was designated for testing purposes (see section II-E2). Consequently, a holdout cross-validation approach was utilized. The training data was partitioned into three subsets: 80% for training, 10% for validation and 10% for testing. Both networks used the same subsets for training. To mitigate overfitting, early stopping was employed, with the validation data being monitored throughout the training process.

TABLE 1. Comparison of training data and test data with the number of perturbation objects, their respective possible conductivities and possible shapes.

	Training Data	Test Data
1 Perturbation	45,000	5,000
2 Perturbations	75,000	5,000
3 Perturbations	130,000	5,000
4 Perturbations	200,000	5,000
5 Perturbations	310,000	5,000
6 Perturbations	-	5,000
7 Perturbations	-	5,000
Conductivities	0, 0.25, 0.75, 1.0	0.0, 0.1, 0.2, 0.3, 0.7, 0.8, 0.9, 1.0
Shapes	Cuboid	Cuboid, Round, L, T

2) TEST DATA

To demonstrate the generalization ability of the neural networks, a separate test dataset was created with more variations in the shape and number of perturbation objects. Additionally, the conductivities were selected from a broader set of conductivities in the range of biological tissue. Each perturbation object was randomly created and could be either in a cuboid, star, L, or T shape. The maximum number of perturbation objects was higher than that of the training data (with up to seven objects). The calculation of signal, noise, and the selection and placement of perturbation objects were conducted in the same manner as in the training data. An overview of the differences between the training and test datasets is provided in Table 1.

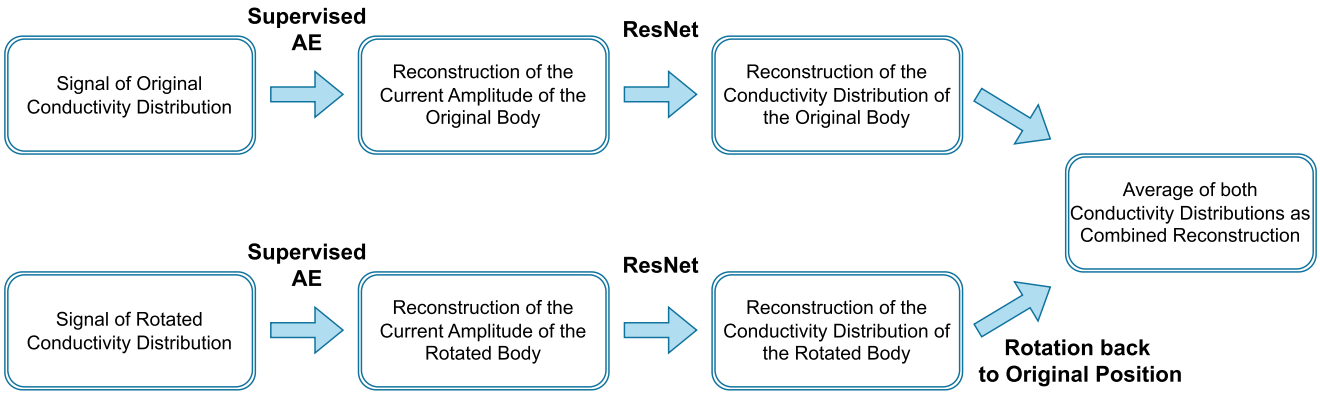

FIGURE 5. Overview of the reconstruction algorithm with two measurements. The first signal is obtained by measuring the original conductivity distribution within the body. First, the current amplitude is reconstructed with a supervised autoencoder from the signals. A residual neural network is employed to predict the conductivity distribution from the current amplitude. The second measurement is of the body rotated by 180 degrees. The conductivity distribution is reconstructed in the same manner as for the first signal. The image reconstruction is then rotated back into the original position. Finally, the mean conductivity value of both reconstructions is calculated for each voxel in order to achieve the final reconstruction of the conductivity distribution.

A further distinction between the training and test data is the utilization of two measurements to reconstruct the conductivity distribution. First, the perturbation objects are randomly positioned, and then the forward problem is calculated. Subsequently, the discretized body is rotated by 180 degrees around the y-axis at the center of the body with a classical rotation matrix. Each voxel is rotated, and the perturbation objects are then on the opposite side of the body. Another forward problem is then calculated, and the resulting signals and current amplitudes of the original and rotated conductivity distribution are saved.

III. RESULTS

Here, the solution of the inverse problem with the proposed subdivision of the problems is tested. The test dataset is used to demonstrate the robustness and generalization ability of the reconstruction process for unknown perturbation shapes and conductivities. Two measurements were employed for each image reconstruction: one of the original conductivity distribution of the body, and the other with the same conductivity distribution rotated by 180 degrees. The reconstruction process was conducted as shown in Fig. 5. Starting from the signals of the original and rotated conductivity distribution, the current amplitudes were reconstructed using the supervised autoencoder. Subsequently, the reconstructed current amplitudes were used to reconstruct the conductivity distribution of both measurements. Finally, one reconstruction was rotated by 180 degrees so that both reconstructions could be combined by calculating the mean value of the conductivity in each voxel.

This combined approach resulted in a reduction in reconstruction errors compared to single reconstructions, as evidenced by Pearson's correlation coefficient in Table 2. Other metrics exhibited comparable trends. In particular, when there are more perturbation objects in the body, the combination of two measurements yields significantly superior results compared with the use of a single measurement. As illustrated in Fig. 6, even when objects are missing in one of the reconstructions, they can appear in the combined result.

A. RECONSTRUCTION OF THE TEST DATASET

The test dataset was created to demonstrate the robustness and generalization capabilities of the proposed inversion algorithm as visualized in Fig. 5. Multiple metrics were calculated to determine the quality of reconstructions of the test samples. Table 3 presents an overview of the metrics used for the entire test dataset.

Fig. 7 shows the reconstruction of a sample from the test dataset, which comprises seven perturbation objects. Although the training data consisted solely of cuboids, each perturbation object was successfully identified. However, their shapes were predominantly reconstructed as cuboids. The conductivities were also within a comparable range to those of the original sample. The reconstructions may appear blurry due to the nature of the magnetic fields used, which does not allow for high-resolution reconstructions.

B. ERROR ANALYSIS AND DISCUSSION

The metrics show the basic trend of the reconstructions; however, a comprehensive error analysis is required to show the strengths and weaknesses of the reconstructions. For this purpose, multiple factors are used, such as the influence of the number of perturbation objects on the metrics.

1) METRICS PER NUMBER OF PERTURBATIONS

Fig. 7 illustrates that more than five perturbation objects can be detected and reconstructed, despite the individual neural networks only being trained on up to five perturbations. However, it should be noted that the metrics may be subject

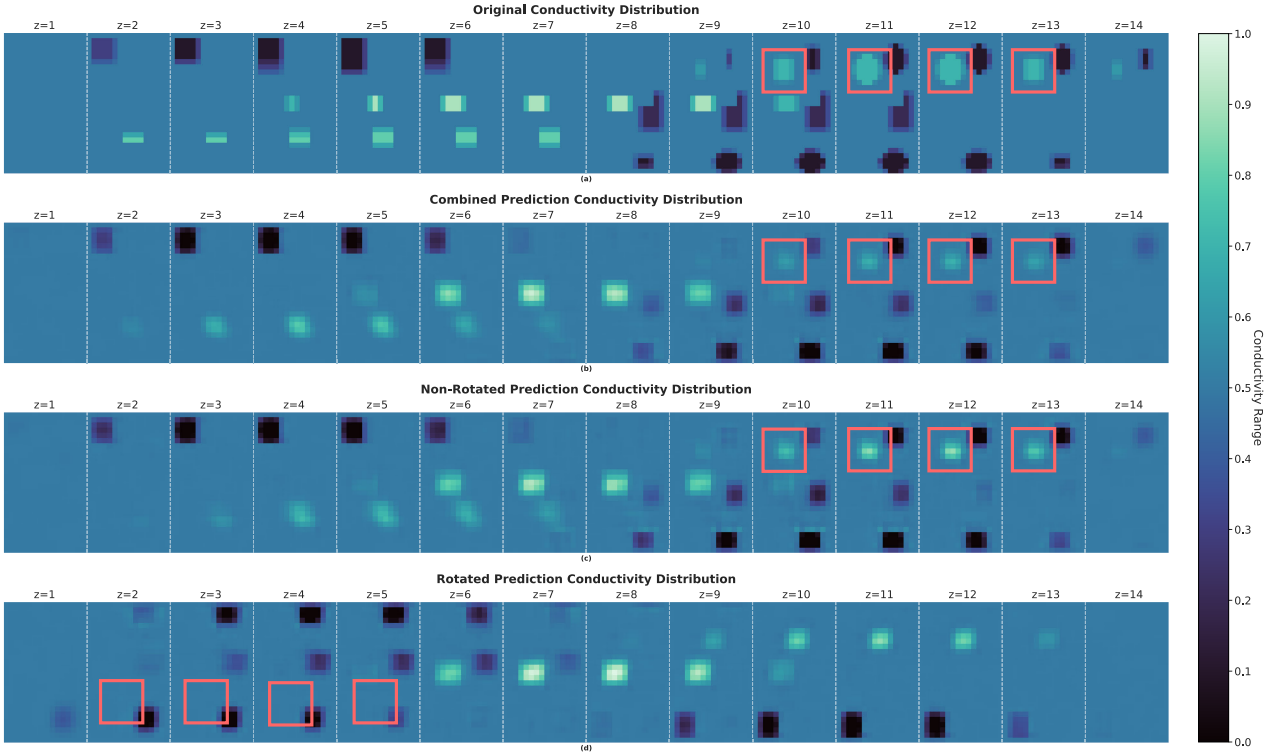

FIGURE 6. Reconstruction comparison of two measurements: In (a), the original conductivity distribution of seven perturbation objects is presented. (b) depicts the reconstructed conductivity distribution, which was obtained by averaging the conductivities presented in figures (c) and (d). (c) depicts the reconstruction of the original body, whereas (d) illustrates the reconstruction conducted using the signal of the rotated body. The reconstruction in (d) is incomplete due to the absence of one of the perturbation objects, indicated by the red border. However, the missing object is visible in (c), and thus it is also reconstructed in the combined reconstruction in (b).

TABLE 2. Pearson score of the test dataset for the combined, original and rotated conductivity distribution.

PEARSON Scores on Test Data	Combined	Original	Rotated
Overall	0.87	0.85	0.85
1 Perturbation	0.91	0.90	0.90
2 Perturbations	0.90	0.88	0.89
3 Perturbations	0.89	0.87	0.87
4 Perturbations	0.88	0.85	0.86
5 Perturbations	0.86	0.83	0.84
6 Perturbations	0.84	0.81	0.81
7 Perturbations	0.82	0.78	0.79

to bias, as the reconstruction of fewer perturbation objects is typically more accurate. Consequently, the metrics were calculated for each number of perturbation objects, with an overview presented in Table 4. The data clearly indicate that an increase in the number of perturbation objects results in a deterioration of the metrics, despite the training data being balanced in favor of more perturbation objects. Nevertheless, despite the use of foreign object shapes and different conductivities, in addition to the increasing number of perturbation objects, the metrics remain within a very good range.

Furthermore, to demonstrate the advantage of using two measurements instead of one, the metrics for the original and rotated measurements were calculated for each

TABLE 3. Comparison of all metric values for the test dataset.

Test Data	PEARSON	SSIM	MAE	MSE
Overall	0.87	0.90	0.009	0.0012

TABLE 4. Comparison of all metric values for each number of perturbation objects.

Test Data	PEARSON	SSIM	MAE	MSE
Overall	0.87	0.90	0.009	0.0012
1 Perturbation	0.91	0.97	0.002	0.0002
2 Perturbations	0.90	0.95	0.004	0.0004
3 Perturbations	0.89	0.93	0.006	0.0007
4 Perturbations	0.88	0.90	0.008	0.0010
5 Perturbations	0.86	0.87	0.011	0.0014
6 Perturbations	0.84	0.84	0.014	0.0019
7 Perturbations	0.82	0.80	0.017	0.0025

perturbation object. As illustrated in Fig. 8, the combination of the two reconstructions resulted in the metrics remaining within a very good range for more perturbation objects. The combined reconstructions demonstrated superior performance compared to single measurement reconstructions as the number of perturbation objects in the samples increased.

2) METRICS PER CONDUCTIVITY VALUE

In addition to the number of perturbation objects, the conductivity values of the perturbation objects can influence

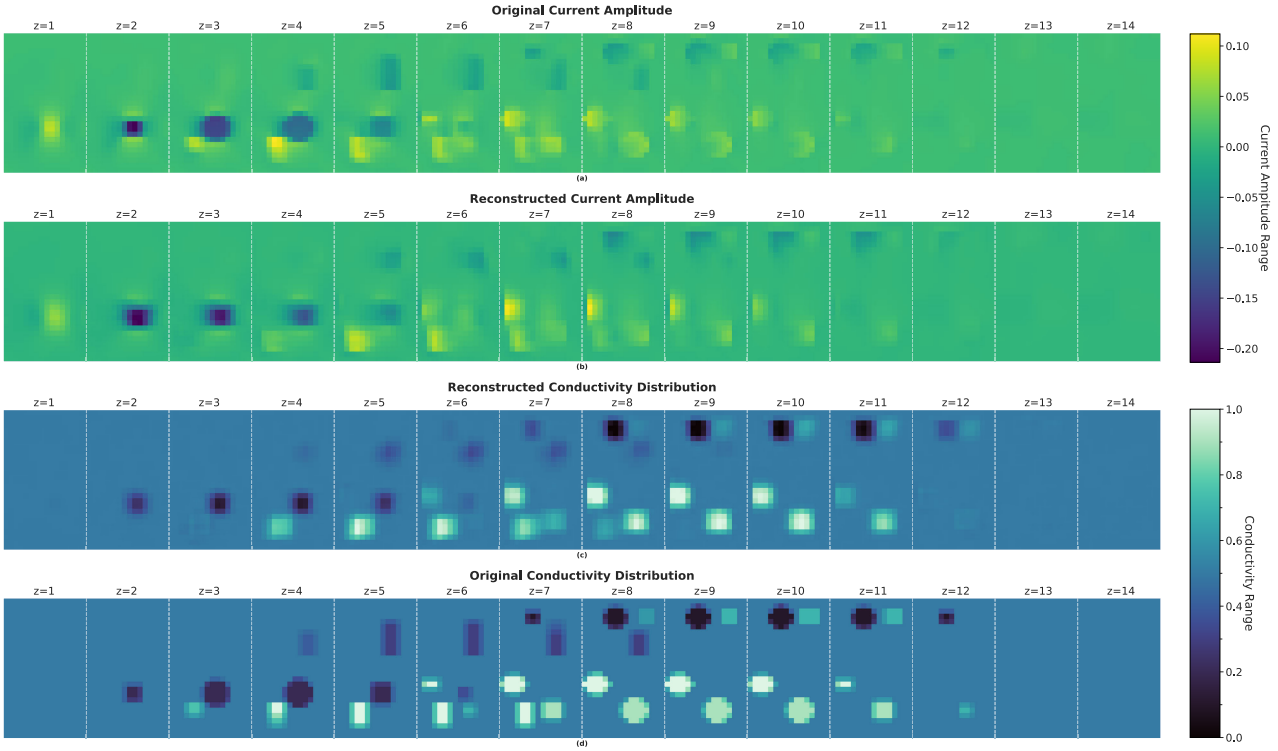

FIGURE 7. Reconstruction of an example of the test dataset, containing seven perturbations and varying shapes and conductivities. In (a), the scaled, original current amplitude is shown, whereas (b) visualizes the reconstruction of the current amplitude from the supervised autoencoder. (c) shows the reconstructed conductivity distribution from the current amplitude in (b). The last figure (d) is the original conductivity distribution.

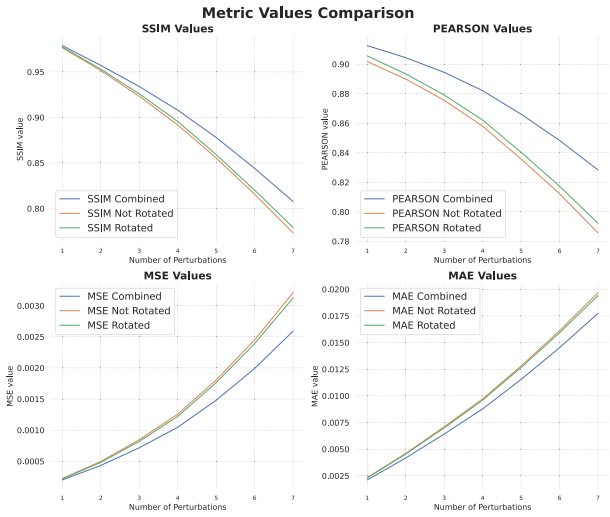

FIGURE 8. Comparison of all metric values for each number of perturbation objects on the test dataset. For each metric, the associated combined metric value and the metrics of the single measurements are shown. The visualization of metrics across the number of perturbation objects demonstrates a clear improvement with the combined reconstructions. This advantage increases with the number of perturbation objects present in the samples.

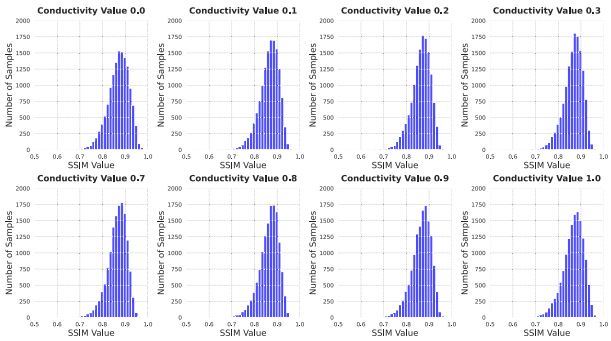

FIGURE 9. SSIM metrics for each conductivity value. Histograms were created for each conductivity value in the test data set. Each histogram displays the number of samples (on the y-axis) for each SSIM value (on the x-axis).

the reconstruction quality. To investigate this, the conductivity values of each perturbation object were saved during the creation of the test dataset. The possible conductivity values were $\sigma \in \{0.0, 0.1, 0.2, 0.3, 0.7, 0.8, 0.9, 1.0\}$ S/m. If a conductivity value was present in the sample of the test dataset, the associated metric values were saved. Fig. 9 illustrates the histograms for each conductivity value, which show the number of samples that achieved the associated SSIM value for each conductivity value. Due to space limitations, only the SSIM value was chosen to be shown here; however, other metrics demonstrated similar behavior.

Overall, all conductivity values demonstrated a tendency towards a slightly skewed normal distribution across all SSIM values, beginning at approximately 0.7 and extending to near 1.0. It appears that perturbation objects with a

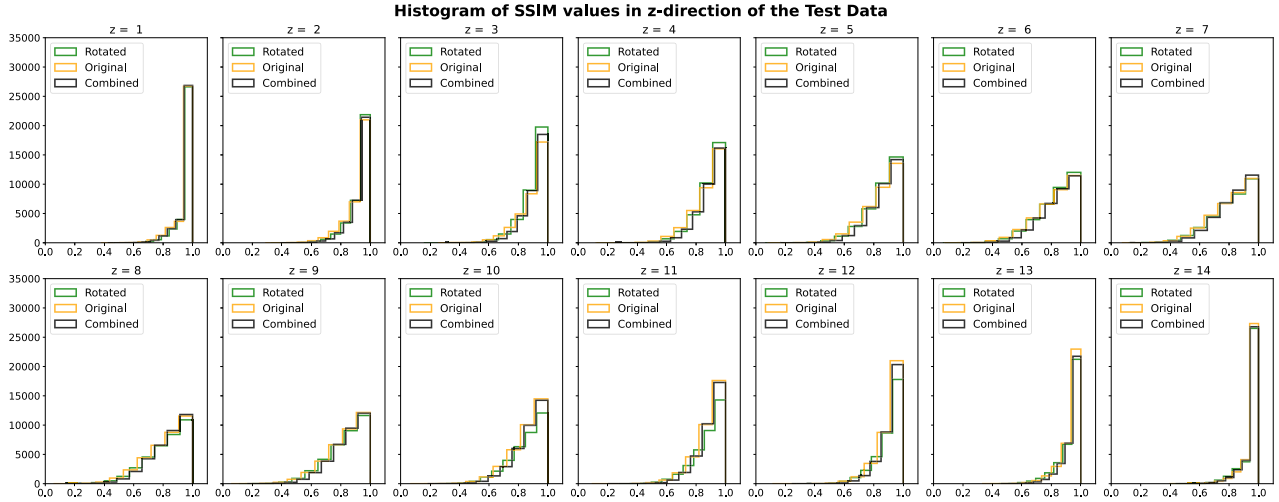

FIGURE 10. SSIM values for each slide in the z-direction of the body. The body was divided into 14 slides in the depth (z-axis) and for each of those slides, the SSIM value was determined. This was done for the combined, original, and rotated reconstructions. For each z-slide, histograms were created, illustrating the distribution of the SSIM values over the test samples.

conductivity of either 0.0 or 1.0 S/m exhibited slightly superior metrics, which was to be anticipated given that these have the greatest contrast to the background conductivity of 0.5 S/m. However, only few reconstructions were overall below a SSIM value of 0.7. No conductivity value was significantly better reconstructed, which indicates that the inverse algorithm demonstrates good generalization capabilities, given that it was only trained on four conductivities.

3) METRICS IN DEPTH

Voluminous magnetic induction tomography often suffers from low central area resolution [5]. Consequently, the reconstruction quality in depth is an important factor to be considered. The body under examination is a voluminous three-dimensional body with the z-direction spanning between the transmitter and the receivers. In order to determine whether specific regions were better reconstructed, the SSIM values for the z-depth were calculated. This entailed determining the SSIM value of each z-slide, which is a two-dimensional slice. In addition, the SSIM values of the reconstructions of the original and rotated single measurements were determined for each z-slide. The rotated reconstructions were rotated back for better comparison. Fig. 10 shows the histograms of the SSIM values across the entire test dataset for each z-slide.

As anticipated, the SSIM values in the regions close to the transmitter or the receivers were significantly higher than those in the central area ($6 \leq z \leq 9$). In these central regions, the combination of the original and rotated measurements resulted in more samples with good metrics than when using single measurements. However, the number of samples exhibiting a very good SSIM value is relatively limited compared with those close to the transmitter and receiver.

As reconstructions are more accurate in close proximity to the receiver, the reconstructions of the non-rotated conductivity distribution have the most samples with very good reconstructions in the z-regions close to the receiver. Conversely, the rotated reconstructions had the greatest number of samples with the most accurate reconstructions in the z-regions closest to the transmitter (which were at the point of measurement closest to the receiver). Therefore, it may be advantageous in the future to combine the reconstructions per z-slide instead of using the naive combined approach employed here. This may result in even more accurate reconstructions. To achieve this, z-slides situated close to the receiver in both measurements could be employed for the outer reconstructions, whereas the combined approach currently in use can be applied to the central area. However, it is essential to thoroughly investigate the correct weighing of the single slides, as the weighting must be independent of the discretization of the body under examination.

IV. CONCLUSION

The proposed two-step inverse algorithm with neural networks demonstrated excellent performance on the test data, which differed significantly from the training dataset. The combination of the two measurements resulted in further improvements in the reconstructions of multiple perturbation objects. However, the current receiver design has its limitations, as occasionally perturbation objects may not be reconstructed, which is barely observed in the metrics. Future research should focus on the construction of new receivers, that can further improve the results. Furthermore, a suitable metric design is required to facilitate more effective comparisons between different receiver settings.

REFERENCES

[1] H.-Y. Wei and M. Soleimani, "Electromagnetic tomography for medical and industrial applications: Challenges and opportunities [point of view]," *Proc. IEEE*, vol. 101, no. 3, pp. 559–565, Mar. 2013.
[2] D. Gürsoy and H. Scharfetter, "Feasibility of lung imaging using magnetic induction tomography," in *Proc. World Congr. Med. Phys. Biomed. Eng.*, Munich, Germany. Berlin, Germany: Springer, Sep. 2009, pp. 525–528.
[3] B. Dekdouk, C. Ktistis, D. W. Armitage, and A. J. Peyton, "Assessing the feasibility of detecting a hemorrhagic type stroke using a 16 channel magnetic induction system," *J. Phys., Conf.*, vol. 224, Apr. 2010, Art. no. 012047.
[4] J. R. Feldkamp and S. Quirk, "Coil geometry effects on scanning single-coil magnetic induction tomography," *Phys. Med. Biol.*, vol. 62, no. 17, pp. 7097–7113, Aug. 2017.
[5] M. Klein, D. Erni, and D. Rueter, "Three-dimensional magnetic induction tomography: Improved performance for the center regions inside a low conductive and voluminous body," *Sensors*, vol. 20, no. 5, p. 1306, Feb. 2020.
[6] M. Ziółkowski, S. Gratkowski, and R. Pałka, "Solution of three dimensional inverse problem of magnetic induction tomography using Tikhonov regularization method," *Int. J. Appl. Electromagn. Mech.*, vol. 30, nos. 3–4, pp. 245–253, Sep. 2009.
[7] M. Soleimani and W. Lionheart, "Image reconstruction in magnetic induction tomography using a regularized Gauss Newton method," in *Proc. 12th Int. Conf. Electr. Bio-Impedance Electr. Impedance Tomogr.*, Jan. 2004, pp. 551–554.
[8] K. H. Jin, M. T. McCann, E. Froustey, and M. Unser, "Deep convolutional neural network for inverse problems in imaging," *IEEE Trans. Image Process.*, vol. 26, no. 9, pp. 4509–4522, Sep. 2017.
[9] E. Kang, J. Min, and J. C. Ye, "A deep convolutional neural network using directional wavelets for low-dose X-ray CT reconstruction," *Med. Phys.*, vol. 44, no. 10, pp. e360–e375, Oct. 2017.
[10] C.-H. Pham, C. Tor-Díez, H. Meunier, N. Bednarek, R. Fablet, N. Passat, and F. Rousseau, "Multiscale brain MRI super-resolution using deep 3D convolutional networks," *Computerized Med. Imag. Graph.*, vol. 77, Oct. 2019, Art. no. 101647.
[11] A. Hofmann, M. Klein, D. Rueter, and A. Sauer, "A deep residual neural network for image reconstruction in biomedical 3D magnetic induction tomography," *Sensors*, vol. 22, no. 20, p. 7925, Oct. 2022.
[12] R. Chen, J. Huang, H. Wang, B. Li, Z. Zhao, J. Wang, and Y. Wang, "A novel algorithm for high-resolution magnetic induction tomography based on stacked auto-encoder for biological tissue imaging," *IEEE Access*, vol. 7, pp. 185597–185606, 2019.
[13] D. Yang, J. Liu, Y. Wang, B. Xu, and X. Wang, "Application of a generative adversarial network in image reconstruction of magnetic induction tomography," *Sensors*, vol. 21, no. 11, p. 3869, Jun. 2021.
[14] T. Schledewitz, M. Klein, and D. Rueter, "Magnetic induction tomography: Separation of the ill-posed and non-linear inverse problem into a series of isolated and less demanding subproblems," *Sensors*, vol. 23, no. 3, p. 1059, Jan. 2023.
[15] J. D. Jackson, *Classical Electrodynamics*, 3rd ed., New York, NY, USA: Wiley, 1999.
[16] C. Altman and K. Suchy, *Reciprocity, Spatial Mapping and Time Reversal in Electromagnetics*. Berlin, Germany: Springer, 2011.
[17] L. Le, A. Patterson, and M. White, "Supervised autoencoders: Improving generalization performance with unsupervised regularizers," in *Proc. Adv. Neural Inf. Process. Syst.*, vol. 31. Red Hook, NY, USA: Curran Associates, Jan. 2018, pp. 107–117.
[18] P. Li, Y. Pei, and J. Li, "A comprehensive survey on design and application of autoencoder in deep learning," *Appl. Soft Comput.*, vol. 138, May 2023, Art. no. 110176.
[19] B. Epstein and R. Meir, "Generalization bounds for unsupervised and semi-supervised learning with autoencoders," 2019, *arXiv:1902.01449*.
[20] K. He, X. Zhang, S. Ren, and J. Sun, "Deep residual learning for image recognition," in *Proc. IEEE Conf. Comput. Vis. Pattern Recognit. (CVPR)*, Jun. 2016, pp. 770–778.

ANNA HOFMANN received the bachelor's and master's degrees in mathematics from the University of Duisburg-Essen, Germany, in 2020. She is currently pursuing the Ph.D. degree in AI and data science with the Graduate School for Applied Research in North Rhine-Westphalia (PKNRW). She is a Research Assistant with the University of Applied Sciences Ruhr West, Mülheim, Germany. Since 2021, she has been researching machine learning methods for magnetic induction tomography as part of an interdisciplinary team of engineers and mathematicians. Her research interests include magnetic induction tomography, include numerical analysis, mathematical optimization, and machine learning.

MORITZ FEHR received the bachelor's degree in geotechnology from the Technical University of Berlin, in 2010, the master's degree in geophysics specializing in seismology from the University of Kiel, and the Ph.D. degree in seismology from the Ruhr University of Bochum, in 2019. After completing the master's degree, he began his professional career, in 2014, as a Geophysicist with DMT GmbH & Co. KG, Essen. There he worked in the field of geomonitoring and vibration measurements. After completing his doctorate degree, he moved to the field of geoinformatics and worked in geodata management. Since February 2022, he has a Research Assistant in the field of data science with the University of Applied Sciences Ruhr West, Mülheim, Germany, where his research focused on the development and programming of neural networks. Since March 2024, he has been a Scientist in research and development in the field of physical measurement technology with Testo SE & Co. KGaA.

ANDREAS SAUER received the Diploma degree in mathematics and computer science and the Ph.D. degree in mathematics from the University of Duisburg, Germany, in 1992 and 1994, respectively, and the Habilitation degree in mathematics, in 2000. Since 2004, he has been a Professor of mathematics with various universities of applied sciences. He has been a Professor of Mathematics at the University of Applied Sciences Ruhr West, Mülheim, Germany, and served as Dean of the Faculty of Natural Sciences from 2012 to 2018. In 2023, he became a member of the Graduate School for Applied Research in North Rhine-Westphalia, focusing on AI and data science. He has authored more than 20 articles in mathematical journals. His research expertise lies in complex analysis. In recent years, his interests have expanded to mathematical problems related to classical physics.